JACS
JOURNAL OF THE AMERICAN CHEMICAL SOCIETY

Article

pubs.acs.org/JACS

Microscopic Investigation of Chemoselectivity in Ag−Pt−Fe_3O_4 Heterotrimer Formation: Mechanistic Insights and Implications for Controlling High-Order Hybrid Nanoparticle Morphology

James M. Hodges, James R. Morse, Mary Elizabeth Williams, and Raymond E. Schaak*

Department of Chemistry and Materials Research Institute, The Pennsylvania State University, University Park, Pennsylvania 16802, United States

Supporting Information

ABSTRACT: Three-component hybrid nanoparticle heterotrimers, which are important multifunctional constructs that underpin diverse applications, are commonly synthesized by growing a third domain off of a two-component heterodimer seed. However, because heterodimer seeds expose two distinct surfaces that often can both support nucleation and growth, selectively targeting one particular surface is critical for exclusively accessing a desired configuration. Understanding and controlling nucleation and growth therefore enables the rational formation of high-order hybrid nanoparticles. Here, we report an in-depth microscopic investigation that probes the chemoselective addition of Ag to Pt−Fe_3O_4 heterodimer seeds to form Ag−Pt−Fe_3O_4 heterotrimers. We find that the formation of the Ag−Pt−Fe_3O_4 heterotrimers initiates with indiscriminate Ag nucleation onto both the Pt and Fe_3O_4 surfaces of Pt−Fe_3O_4, followed by surface diffusion and coalescence of Ag onto the Pt surface to form the Ag−Pt−Fe_3O_4 product. Control experiments reveal that the size of the Ag domain of Ag−Pt−Fe_3O_4 correlates with the overall surface area of the Pt−Fe_3O_4 seeds, which is consistent with the coalescence of Ag through a surface-mediated process and can also be exploited to tune the size of the Ag domain. Additionally, we observe that small iron oxide islands on the Pt surface of the Pt−Fe_3O_4 seeds, deposited during the formation of Pt−Fe_3O_4, define the morphology of the Ag domain, which in turn influences its optical properties. These results provide unprecedented microscopic insights into the pathway by which Ag−Pt−Fe_3O_4 heterotrimer nanoparticles form and uncover new design guidelines for the synthesis of high-order hybrid nanoparticles with precisely targeted morphologies and properties.

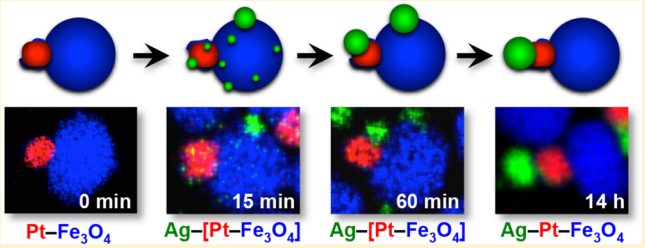

INTRODUCTION

Colloidal hybrid nanoparticles, which integrate two or more nanocrystals into a one-particle system, are highly tunable, multifunctional materials that can facilitate unique applications in biomedical imaging,[1] solar-energy harvesting,[2−4] heterogeneous catalysis,[5−7] photonics,[8,9] optics[10,11] and electronics.[12,13] The physical and chemical properties of hybrid nanomaterials are defined in part by their heterointerfaces, which can enable electronic[14,15] and magnetic[16−18] coupling between the constituent domains and therefore allow for functionalities that are not possible in single-component systems. The most widely studied class of hybrid nanoparticles are two-component heterodimers, although high-order hybrid systems, which contain three or more nanocrystal domains, offer greater multifunctionality and more sophisticated synergistic properties and applications. For example, photocatalytic water splitting is enabled by three-component heterotrimer nanoparticles that contain a light-absorbing domain attached to a hydrogen-evolving catalyst on one side and an oxygen-evolving catalyst on the other.[19] Likewise, Au−MnO−SiO_2 hybrid nanoparticles offer enhanced multifunctionality and greater biocompatibility, relative to two-component Au−MnO heterodimers, which ultimately enable advanced theranostic applications.[20]

Underpinning the construction of high-order colloidal hybrid nanoparticles, including the heterotrimer systems mentioned above, are reliable synthetic methods that produce the target hybrid constructs in high yields and with precise configurations, interfaces, and spatial arrangements. Such hybrid nanoparticle systems are typically synthesized using sequential seeded-growth methods, where preformed nanoparticles are used as seeds for growing additional domains in subsequent reactions. These stepwise reaction sequences are conceptually analogous to the total synthesis methodology used by organic chemists to synthesize large, complex molecules.[21] While the organic reactions that underpin molecular total synthesis can be applied rationally in a by-design manner, the rules and guidelines for constructing high-order hybrid nanoparticles are poorly understood and far from mature. For example, heterotrimers such as the prototype system Ag−Pt−Fe_3O_4 are synthesized by growing Ag off of the Pt domain of Pt−Fe_3O_4 heterodimer seeds, and this seeded-growth reaction is considered to be chemoselective.[22] Ag readily grows on both Pt and Fe_3O_4 nanoparticles individually to form Pt@Ag core−

Received: September 30, 2015
Published: November 24, 2015

DOI: 10.1021/jacs.5b10254
J. Am. Chem. Soc. 2015, 137, 15493−15500

shell nanoparticles and Ag−Fe_3O_4 heterodimers, respectively.[22] However, when growing Ag on Pt−Fe_3O_4 heterodimer seeds where both the Pt and Fe_3O_4 surfaces are exposed and accessible, Ag will grow exclusively from the Pt surface to form Ag−Pt−Fe_3O_4 rather than alternate products such as Pt−Fe_3O_4−Ag or Ag−Pt−Fe_3O_4−Ag, which control experiments suggest should also be accessible.[22]

Such chemoselective behavior is observed in a growing number of heterotrimer syntheses.[22−24] While chemical driving forces such as maximization of interfacial bond energies[24−26] and electronic effects[22] have been postulated to underpin the observed chemoselective growth, experimental evidence remains elusive and, as a result, the process remains poorly understood. Such mechanistic knowledge is important, because ultimately it enables our ability to select and control which surfaces of multiparticle constructs facilitate additional particle growth. This, in turn, makes it possible to deterministically control configurational isomerism in high-order hybrid nanoparticles, which is a prerequisite for designing and precisely synthesizing, in high yield, multicomponent nanostructures with targeted interfaces and spatial arrangements and, consequently, synergistic functions.[23,27]

In this contribution, we describe the results of a high-resolution microscopic investigation into the formation of Ag−Pt−Fe_3O_4 heterotrimers from Pt−Fe_3O_4 heterodimer seeds, as well as their synthetic implications, which could lead to significant new design capabilities. Specifically, we show that the chemoselective addition of Ag onto Pt−Fe_3O_4 heterodimer seeds occurs first through indiscriminate Ag nucleation, where Ag nucleates on *both* the Pt and Fe_3O_4 surfaces, followed by coalescence of Ag onto the Pt domain to form the Ag−Pt−Fe_3O_4 heterotrimer product. The observation that Ag relocates to the Pt surface provides compelling experimental evidence that the observed chemoselective behavior is driven by the formation of a more favorable Ag−Pt interface, relative to that of Ag−Fe_3O_4. Additionally, control studies reveal that the volume of the Ag domain in the heterotrimer product is proportional to the overall surface area of the Pt−Fe_3O_4 heterodimer seeds, which is consistent with a surface-mediated Ag diffusion and coalescence mechanism. Furthermore, these insights help to rationalize observations of polydispersity in the sizes of the Ag domains of Ag−Pt−Fe_3O_4 heterotrimers and provide guidelines for achieving more monodisperse samples. We also provide experimental evidence that small iron oxide islands on the Pt surface, which are formed during the Pt−Fe_3O_4 heterodimer synthesis, are responsible for producing a Ag domain morphology on the Ag−Pt−Fe_3O_4 heterotrimer product that is different than the related Pt@Ag core−shell nanoparticles. This, in turn, influences the plasmonic properties of the material. Such mechanistic insights have significant implications for controlling subtle, yet important, morphological characteristics of the heterotrimer products that directly impact their functions.

EXPERIMENTAL SECTION

Materials. Oleylamine (OLAM; technical grade, 70%), oleic acid (OLAC; technical grade, 90%), 1-octadecene (ODE; technical grade, 90%), platinum(II) acetylacetonate [$Pt(acac)_2$; 97%], iron(0) pentacarbonyl [$Fe(CO)_5$; >99.99%], silver(I) acetate [$Ag(C_2H_3O_2)$; anhydrous, 99%], gold(III) chloride trihydrate ($HAuCl_4{\cdot}3H_2O$; 99%), and borane *tert*-butylamine (TBAB; 97%) were purchased from Sigma-Aldrich. Iron(III) acetylacetonate [$Fe(acac)_3$; 99%] was purchased from STREM Chemicals. Iron(III) chloride hexahydrate ($FeCl_3{\cdot}6H_2O$; 97%) was purchased from Alfa Aesar. Sodium oleate (97%) was purchased from TCI Chemicals. Solvents, including toluene, hexanes, 2-propanol, and ethanol, were of analytical grade. All chemicals were used as received.

Synthesis of Ag−Pt−Fe_3O_4. Pt and Pt−Fe_3O_4 seed particles were synthesized using modified versions of published procedures (detailed synthetic procedures for these samples can be found in the Supporting Information).[28] Ag−Pt−Fe_3O_4 was also prepared through a modified procedure.[29] $Ag(C_2H_3O_2)$ (36 mg) was dissolved in a solution of toluene (10 mL) and OLAM (3.75 mL) that contained Pt−Fe_3O_4 nanoparticle seeds (8 mg) in a 50 mL three-necked round-bottom flask equipped with a thermocouple, gas flow adapter, rubber septum, and magnetic stir bar. The reaction was held under vacuum for 2 min at room temperature and then heated to 65 °C under an Ar blanket and left for 14 h. Aliquots of the reaction were removed at 15 and 60 min after the reaction reached 65 °C. Both aliquots and the final product were cooled to room temperature and precipitated with ethanol and then isolated by centrifugation. All samples were then redispersed in hexanes, and the washing procedure was repeated two more times. The final nanoparticle samples were redispersed in hexanes with 0.5% OLAM and 0.5% OLAC by volume.

Synthesis of Bimodal Ag−Pt−Fe_3O_4. Pt−Fe_3O_4 seeds were first synthesized through an alternate literature procedure than the one described above, which allowed for Pt−Fe_3O_4 with varying Fe_3O_4 domain sizes.[30] Two parallel reactions were run with identical Pt seeds to generate two Pt−Fe_3O_4 samples with Fe_3O_4 diameters of 10 ± 2 and 15 ± 2 nm, respectively. Synthetic details for the bimodal Pt−Fe_3O_4 seeds are provided in the Supporting Information. Bimodal Ag−Pt−Fe_3O_4 was then generated through the same synthetic procedure described above for the Ag−Pt−Fe_3O_4, using a 1:1 mixture of the two Pt−Fe_3O_4 samples and 13 mg of $Ag(C_2H_3O_2)$ (instead of 36 mg).

Synthesis of Bimodal Ag−Fe_3O_4. Two distinct Fe_3O_4 nanoparticle seed populations, one having an average diameter of 16 ± 2 nm and the other having an average diameter of 24 ± 2 nm, were synthesized following a modified procedure previously reported by Park et al.[31] using iron oleate. Detailed synthetic procedures are described in the Supporting Information. To synthesize the bimodal population of Ag−Fe_3O_4 heterodimers, $Ag(C_2H_3O_2)$ (36 mg) was mixed with a solution of toluene (10 mL), OLAM (3.75 mL), and a mixture of the 16 ± 2 and 24 ± 2 nm Fe_3O_4 nanoparticles (4 mg each) in a 50 mL, three-necked round-bottom flask equipped with a thermocouple, gas flow adapter, rubber septum, and magnetic stir bar. The same reaction conditions and washing steps were used for the Ag−Pt−Fe_3O_4 nanoparticles described above.

Synthesis of Pt@Ag Core−Shell Particles. The same procedure described in the "Synthesis" of Ag−Pt−Fe_3O_4 section was followed, except that Pt nanoparticle seeds (8 mg) were used instead of Pt−Fe_3O_4.

Characterization. Transmission electron microscopy (TEM) images were collected with a JEOL 1200 EX II microscope operating at 80 kV. High-resolution TEM (HRTEM) images, high-angle annular dark-field scanning TEM (HAADF-STEM) images, and STEM energy dispersive X-ray spectroscopy (STEM-EDS) maps were collected with an FEI Titan^3 G2 S/TEM equipped with spherical aberration correctors on the image and probe-forming lenses at an accelerating voltage of 200 kV. EDS maps were acquired with the FEI Titan^3 using the Super-X EDX quad detector system at a current of ∼0.15 nA. Standardless Cliff− Lorimer quantification was performed on the deconvoluted EDS line intensity data using the Bruker Esprit software. ES Vision software (Emispec) was used for EDS data processing. Specific samples, as noted in the text, were magnetically purified with differential magnetic catch and release (DMCR)[32,33] using a 250 μm inner diameter silica capillary, 10 μL/min solvent flow rate, and 1.8 T magnetic flux (see the Supporting Information for more details). Particle sizing was determined using ImageJ software by measuring >100 particles per sample. Powder X-ray diffraction (XRD) patterns were collected with a Bruker Advance D8 X-ray diffractometer and Cu Kα radiation at room temperature. Simulated powder XRD patterns were made using the CrystalMaker and CrystalDiffract software suite. UV/visible absorbance spectra were obtained for dilute nanoparticle

DOI: 10.1021/jacs.5b10254
J. Am. Chem. Soc. 2015, 137, 15493−15500

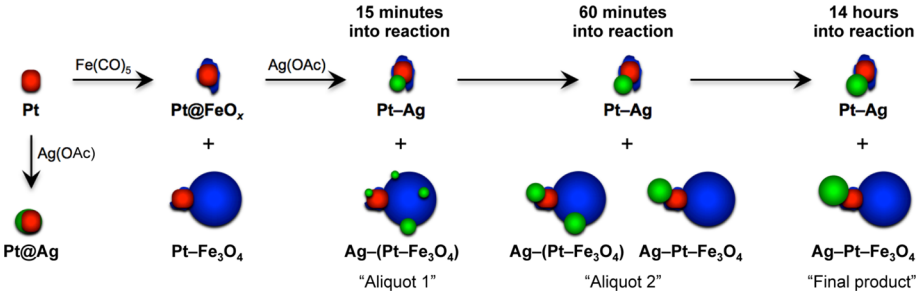

Figure 1. Schematic representation of the stepwise reaction sequences used to synthesize Ag–Pt–Fe_3O_4 heterotrimers, Pt–Ag heterodimers, and Pt@Ag core–shell nanoparticles; each product and aliquot are described and referred to in the text. Aliquots taken at 15 and 60 min into the Ag–Pt–Fe_3O_4 reaction reveal a Ag–(Pt–Fe_3O_4) intermediate, where Ag domains are attached to both the Pt and Fe_3O_4 surfaces of the Pt–Fe_3O_4 seeds.

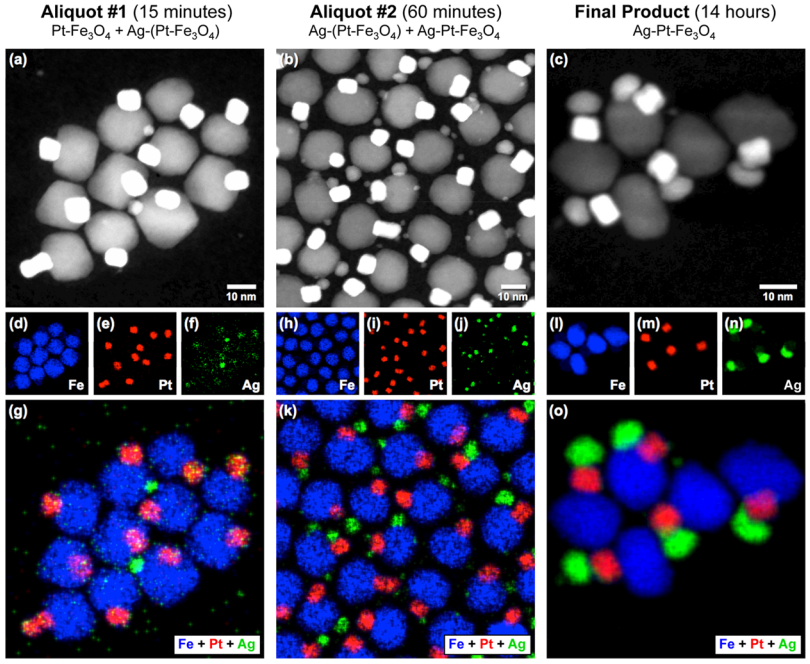

Figure 2. Representative HAADF-STEM images of aliquot samples taken from the Ag–Pt–Fe_3O_4 synthesis at (a) 15 min and (b) 60 min into the reaction, as well as (c) the final Ag–Pt–Fe_3O_4 heterotrimer product isolated after 14 h. The corresponding EDS elemental maps are shown in panels d–g, h–k, and l–o, respectively, and indicate that Ag indiscriminately nucleates on the Pt–Fe_3O_4 heterodimers to form various Ag–(Pt–Fe_3O_4) intermediates, followed by coalescence onto the Pt domain to form Ag–Pt–Fe_3O_4.

samples suspended in hexanes using a Varian Cary 500 double-beam spectrophotometer with 1 cm quartz cuvette sample holders.

RESULTS AND DISCUSSION

Microscopic Investigation of Chemoselective Ag–Pt–Fe_3O_4 Heterotrimer Formation. Pt–Fe_3O_4 heterodimers were synthesized by reacting $Fe(CO)_5$ with Pt seeds in ODE as reported previously.[28] Characterization of the Pt–Fe_3O_4 heterodimers, as well as the Pt nanoparticle seeds, is included in Figure S1 (Supporting Information). In order to elucidate the pathway by which Ag nanocrystals nucleate and grow chemoselectively on Pt–Fe_3O_4 heterodimer seeds to form Ag–Pt–Fe_3O_4 heterotrimer products, aliquots taken during various stages of the synthesis were studied to capture and analyze the reaction intermediates. To synthesize the Ag–Pt–Fe_3O_4 heterotrimer nanoparticles, the Pt–Fe_3O_4 heterodimers were reacted with a solution of $Ag(C_2H_3O_2)$ in toluene and oleylamine at 65 °C for 14 h.[27] To probe the early stages of the reaction, aliquots were removed at 15 and 60 min into the 14-h process. Each sample contained populations of unreacted Pt seeds and free Ag nanocrystals, as well as other byproducts. Therefore, DMCR,[32,33] which separates hybrid nanoparticles containing magnetic Fe_3O_4 domains from those that do not, was used to purify each sample, enriching the sample in the heterotrimer product and enabling explicit characterization of that mechanistically relevant subpopulation (see the Supporting Information for details). Figure 1 shows a schematic of the synthesis and aliquot processes, as well as depictions of and labels for the various components of each sample, as will be described and referred to in the paragraphs that follow.

Parts a, b, and c of Figure 2 respectively show HAADF-STEM images of all three samples—the 15 min aliquot, the 60 min aliquot, and the final product after the 14-h reaction—after DMCR purification, where the primary product includes connected Ag, Pt, and Fe_3O_4 nanoparticle domains. The corresponding larger-area bright-field TEM images are shown in Figure S2 of the Supporting Information. The aliquot samples taken at 15 and 60 min into the reaction, which are shown in parts a and b of Figure 2, respectively, clearly show small particles decorating both the Pt and Fe_3O_4 surfaces of the Pt–Fe_3O_4 heterodimer seeds. After 14 h, as shown in Figure 2c, the final nanoparticle product has the anticipated Ag–Pt–

DOI: 10.1021/jacs.5b10254
J. Am. Chem. Soc. 2015, 137, 15493–15500

Fe_3O_4 heterotrimer architecture that is consistent with previous reports.[22] To determine the identities of each of the domains in the hybrid nanoparticle products, STEM-EDS was used to construct elemental maps of each sample. The STEM-EDS maps for the aliquot taken after 15 min (Figure 2d–g), which correspond to the HAADF-STEM image shown in Figure 2a, clearly show small Ag nanoparticles attached to both the Pt and Fe_3O_4 surfaces of the Pt–Fe_3O_4 heterodimer seeds [denoted as Ag–(Pt–Fe_3O_4)], as well as Pt–Fe_3O_4 heterodimers having no detectable Ag. After 60 min, the number and size of the Ag nanoparticles growing on the Pt–Fe_3O_4 seeds has increased, and the formation of Ag–Pt–Fe_3O_4 heterotrimers has initiated, as indicated by the STEM-EDS maps shown in Figure 2h–k. The STEM-EDS maps shown in Figure 2l–o confirm that after 14 h the final nanoparticle product is indeed the expected Ag–Pt–Fe_3O_4 heterotrimer configuration. The HRTEM images in parts a and b of Figure S3 (Supporting Information) further confirm the identity and location of the Ag domain on the predominant species in aliquot 2 [Ag–(Pt–Fe_3O_4)] and the final 14-h product [Ag–Pt–Fe_3O_4], respectively. These observations suggest that the chemoselective growth of Ag on Pt–Fe_3O_4 heterodimers does not occur through domain-selective nucleation, but rather indiscriminate nucleation of Ag onto both exposed surfaces of the Pt–Fe_3O_4 nanoparticle seeds—forming Ag–(Pt–Fe_3O_4) intermediates—followed by coalescence onto the Pt domain.

To further characterize the Ag–(Pt–Fe_3O_4) intermediates that were presented in Figure 2b, higher-magnification STEM-EDS maps and lower-magnification HAADF-STEM images were obtained. Figure 3a shows a HAADF-STEM image of two isolated particles from the 60 min aliquot sample, and parts b and c of Figure 3 show, respectively, the corresponding STEM-EDS maps for Ag and an overlay of Ag, Pt, and Fe. These HAADF-STEM and STEM-EDS images clearly show several Ag domains attached to both the Pt and Fe_3O_4 surfaces. A low-magnification HAADF-STEM image of the same 60-min aliquot, shown in Figure S4 (Supporting Information), also clearly shows small Ag nanocrystals indiscriminately growing on a large population of Pt–Fe_3O_4 seeds. Note that because these images were collected for samples isolated after DMCR purification, the particles as a whole are superparamagnetic, which means that the Ag present in these samples should be attached to the Fe_3O_4 domain in order to be retained in the magnetically purified product. The data presented thus far further support the conclusion that the chemoselective addition of Ag to Pt–Fe_3O_4 occurs through multiple Ag nucleation events, followed by coalescence onto the Pt domain to form the final Ag–Pt–Fe_3O_4 heterotrimer product. The preference for the final Ag–Pt–Fe_3O_4 configuration is not unexpected, as Pt and Ag have identical crystal structures (face-centered cubic) and the deposition of Ag has been shown to induce a pseudomorphic, monolayer-confined alloy at the Pt surface.[34,35] However, directly observing the intermediate nanostructures associated with this formation pathway helps to more explicitly define the process by which the heterotrimers form and, as a consequence, has implications for more rationally controlling important morphological features of high-order hybrid nanoparticles.

Previous reports of chemoselective growth in high-order hybrid nanoparticle syntheses have suggested that electronic interactions across the heterointerfaces could facilitate polarization effects in the heterodimer seeds, which in turn could facilitate site-selective nucleation.[21] Analogous electronic effects

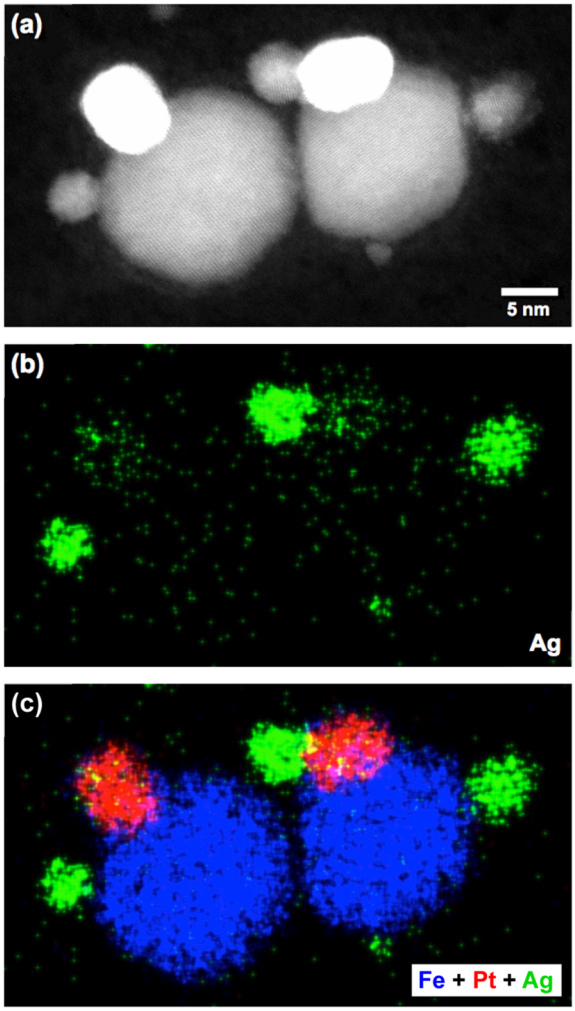

Figure 3. (a) High-magnification HAADF-STEM image showing a representative Ag–(Pt–Fe_3O_4) intermediate from the aliquot taken at 60 min into the Ag–Pt–Fe_3O_4 reaction. The nanoparticles display small domains attached to the Pt and Fe_3O_4 surfaces of the Pt–Fe_3O_4 seeds, which are confirmed to be Ag in the corresponding EDS elemental maps shown in parts b and c.

have been implicated in the enhanced catalytic properties observed for Pt–Fe_3O_4 heterodimers relative to morphologically comparable Pt nanoparticles.[7,28] In contrast, the microscopy data presented here provide compelling experimental evidence in favor of a pathway involving indiscriminate, multisite nucleation followed by surface migration, which was proposed by Cao and co-workers to rationalize the formation of UO_2–In_2O_3 and FePt–In_2O_3 heterodimer nanoparticles.[25] After multiple small Ag clusters nucleate onto both exposed domains of the Pt–Fe_3O_4 surface, the Ag undergoes intraparticle coalescence to reduce the overall surface energy of the Ag domain. Sun and co-workers observed a similar phenomenon while studying the Ag–Fe_3O_4 heterodimer system,[36] which is further corroborated by our findings in the higher-order Ag–Pt–Fe_3O_4 heterotrimer system. During intraparticle coalescence, any Ag on the Fe_3O_4 surface is significantly less stable due to the chemical and crystal dissimilarities of the two materials. As the synthesis proceeds, Ag migrates across the hybrid nanoparticle surface, eventually reaching the exposed surface of the Pt domain to form a more favorable interface and provide a stable anchor for further Ag growth. These

DOI: 10.1021/jacs.5b10254
J. Am. Chem. Soc. 2015, 137, 15493–15500

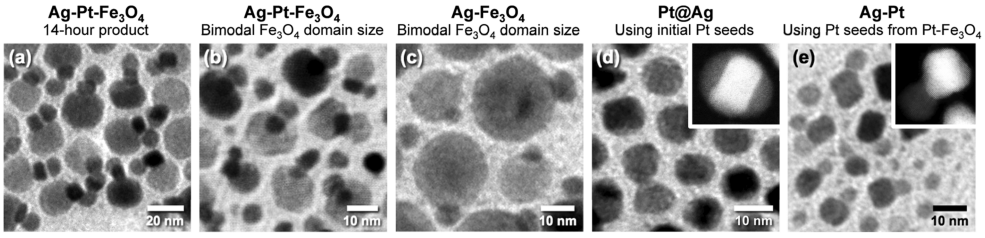

Figure 4. Representative TEM images of (a) Ag–Pt–Fe_3O_4 heterotrimers that have uniform Fe_3O_4 domains and accordingly uniform Ag domains, (b) Ag–Pt–Fe_3O_4 heterotrimers generated from Pt–Fe_3O_4 seeds that have a bimodal distribution of Fe_3O_4 sizes and accordingly bimodal Ag domain sizes, (c) Ag–Fe_3O_4 heterodimers generated from Fe_3O_4 seeds that have a bimodal distribution of sizes and accordingly bimodal Ag domain sizes, (d) Pt@Ag core–shell nanoparticles synthesized using the as-made Pt seeds, and (e) Ag–Pt heterodimers synthesized using the Pt seeds after deposition of iron oxide surface deposits as occurred during the formation of Pt–Fe_3O_4 heterodimers.

mechanistic insights are useful for rationalizing the origin of the observed chemoselective nanoparticle growth in high-order hybrid nanoparticle synthesis, where multiple reasonable possibilities may be postulated. Importantly, they also provide insights into the origin of more subtle morphological features that impact their properties, which can be leveraged and exploited in the design and synthesis of more sophisticated and tunable higher-order heterostructures, as described in the sections that follow.

Implications for Morphology Control in High-Order Hybrid Nanoparticles. Figure 4 shows TEM images of five distinct nanoparticle samples that were generated by growing Ag nanoparticles off of a variety of nanoparticle or hybrid nanoparticle seeds. The sample shown in Figure 4a represents a typical Ag–Pt–Fe_3O_4 heterotrimer product, which was formed through the seeded growth of Ag off of a single as-made sample of Pt–Fe_3O_4 heterodimers, identical to the final product of the 14-h reaction described above. Figure 4b shows a different sample of Ag–Pt–Fe_3O_4 heterotrimers synthesized using Pt–Fe_3O_4 heterodimer seeds that have a wider range of Fe_3O_4 nanoparticle diameters and are therefore significantly more polydisperse than the Pt–Fe_3O_4 seeds used to synthesize the Ag–Pt–Fe_3O_4 heterotrimers in Figure 4a. Inspection of the Ag–Pt–Fe_3O_4 sample in Figure 4b and comparison with that in Figure 4a suggest that the average sizes of the Ag domains may correlate with the average sizes of the Fe_3O_4 domains: the Ag–Pt–Fe_3O_4 heterotrimers have larger Ag domains when the Fe_3O_4 domains of the Pt–Fe_3O_4 heterodimer seeds are larger. Consistent with this, Figure 4c shows Ag–Fe_3O_4 heterodimers synthesized from a bimodal population of Fe_3O_4 nanoparticle seeds, and the larger Fe_3O_4 domains again contain the larger Ag domains. Figure 4d shows the product of Ag growth directly off of the Pt seeds that are used in forming Pt–Fe_3O_4 heterodimers. Here, as observed previously, the Ag conformally coats most of the Pt surface in a core–shell architecture, as confirmed by the STEM-EDS element map in Figure S5 (Supporting Information). The Pt@Ag heterostructures in Figure 4d contrast those in Figure 4e, which show a distinct hybrid nanoparticle architecture. The Ag–Pt heterodimers shown in Figure 4e are a byproduct of the Ag–Pt–Fe_3O_4 synthesis, whereby unreacted Pt nanoparticles from the Pt–Fe_3O_4 heterodimer sample react with the Ag precursor. (These Ag–Pt heterodimer byproducts in Figure 4e were part of the Ag–Pt–Fe_3O_4 product prior to DMCR purification, as shown schematically in Figure 1; since they do not contain a magnetic Fe_3O_4 domain, they were not present in the aliquot samples that were shown in Figures 1 and 2.) The Ag–Pt–Fe_3O_4 heterotrimer formation pathway that was identified microscopically and discussed in the previous section, involving a multisite nucleation and surface diffusion process, is consistent with, and helps to rationalize, the different Ag sizes and morphologies that are observed in Figure 4, as described in more detail below. Collectively, these observations provide significant new design guidelines for controlling subtle, yet important, features of high-order nanoparticle morphology.

To test the hypothesis that the size of the Ag domain in the Ag–Pt–Fe_3O_4 heterotrimer product correlates with the size of the Fe_3O_4 domains in the Pt–Fe_3O_4 heterodimers seeds, which would be consistent with a surface-mediated Ag coalescence process as mentioned above, Pt–Fe_3O_4 nanoparticles with a bimodal distribution of Fe_3O_4 domain sizes were prepared. Briefly, Pt–Fe_3O_4 heterodimers with Fe_3O_4 domain sizes of 15 ± 2 and 10 ± 2 nm were prepared separately in two distinct reactions that used different ratios of Pt nanoparticles with $Fe(acac)_3$, as described in detail in the Experimental Section. The two samples with heterodimers containing distinct Fe_3O_4 domain sizes were mixed in equal amounts to produce a single sample having a bimodal population of Pt–Fe_3O_4 particles and then reacted with $Ag(C_2H_3O_2)$ to form Ag–Pt–Fe_3O_4, as described previously. A representative TEM image of the resulting polydisperse Ag–Pt–Fe_3O_4 sample and a scatterplot correlating the diameters of the Ag and Fe_3O_4 domains of >150 Ag–Pt–Fe_3O_4 heterotrimer particles are shown in parts a and b of Figure 5, respectively. The analysis in Figure 5b reveals that the sizes of the Ag domains in the Ag–Pt–Fe_3O_4 heterotrimer product are indeed proportional to the sizes of the Fe_3O_4 domains. Because the diameters of the nanoparticle domains also are proportional to their surface areas, and because the

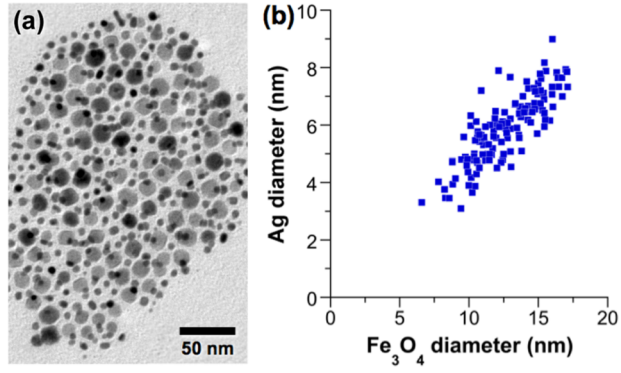

Figure 5. (a) Representative TEM image of Ag–Pt–Fe_3O_4 heterotrimers with bimodal size distributions of Ag and Fe_3O_4 domains. (b) The corresponding scatterplot that shows that large Fe_3O_4 domains correlate with larger Ag domains, suggesting that Ag coalescence is a surface-mediated process.

DOI: 10.1021/jacs.5b10254
J. Am. Chem. Soc. 2015, 137, 15493–15500

sizes of the Pt domains do not vary significantly, we can conclude that the volume of the Ag domain correlates with the total surface area of the Pt−Fe_3O_4 seed particles. This analysis further validates the proposed surface-mediated coalescence pathway, since a larger exposed surface area would support more nucleation events and/or a larger amount of adsorbed Ag, which in turn would lead to a larger final Ag domain after surface diffusion and coalescence.

The above analysis revealed that the size of the Fe_3O_4 domain in the Pt−Fe_3O_4 heterodimer seeds is a key parameter that influences the size and uniformity of the Ag domain. Consistent with this, when a bimodal population of Fe_3O_4 nanoparticles is used as seeds for the nucleation and growth of Ag (without the presence of a Pt domain), the larger Fe_3O_4 nanoparticles produce Ag−Fe_3O_4 heterodimer products having larger Ag domains (Figure 6a) and the smaller Fe_3O_4 nanoparticles produce Ag−Fe_3O_4 heterodimer products having smaller Ag domains (Figure 6b); additional TEM images are shown in Figure S6 of the Supporting Information. The corresponding scatterplot in Figure 6c shows that two distinct populations of Ag domains exist and also that they correlate with the sizes of the Fe_3O_4 domains to which they are interfaced. Likewise, the histograms showing the distributions of Fe_3O_4 and Ag domain diameters, included in Figure S7 (Supporting Information), confirm the coexistence of two statistically distinct size populations. Ridelman et al. similarly observed that Fe_3O_4 seed size directly influences the size of the Ag domains in colloidally synthesized Ag−Fe_3O_4 heterodimers.[37] These results provide compelling evidence that polydispersity in the Fe_3O_4 domains leads to polydispersity in the nanoparticle domains that are grown off of them, whether the subsequently grown domain is directly connected to it (as in the case of forming Ag−Fe_3O_4 from Fe_3O_4) or not (as in the case of forming Ag−Pt−Fe_3O_4 from Pt−Fe_3O_4). The observation that the morphological characteristics of the domains within a heterodimer seed can influence the morphological characteristics of a larger heterotrimer product through a surface-area-limited process has important implications for designing high-order hybrid nanoparticle systems with highly controllable features, ultimately suggesting that monodispersity begets monodispersity: the uniformity of the first seeded growth step dictates the uniformity of a subsequent step.

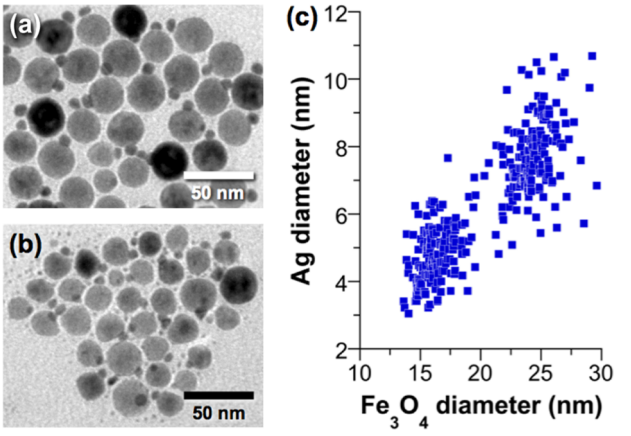

Figure 6. Representative TEM images of Ag−Fe_3O_4 heterodimers generated by growing Ag from (a) 24 nm Fe_3O_4 seeds and (b) 16 nm Fe_3O_4 seeds. (c) The scatterplot that shows two distinct Ag populations, which correlate with the bimodal Fe_3O_4 seeds; larger Fe_3O_4 domains facilitate the formation of larger Ag domains.

In addition to a direct correlation between Ag and Fe_3O_4 domain sizes, Figure 4 also reveals two morphologically distinct types of Ag−Pt heterostructures: one with a core−shell architecture (Figure 4d) and one with a two-lobe heterodimer morphology (Figure 4e). As was noted in the schematic in Figure 1, the two types of Ag−Pt heterostructures emerge from subtly different Pt nanoparticle seeds. The Pt@Ag heterostructures with a core−shell architecture form from the reaction of the as-synthesized Pt nanoparticle seeds with $Ag(C_2H_3O_2)$, without any Fe-containing reagents or nanoparticles present, while the Ag−Pt heterodimers form from the reaction of $Ag(C_2H_3O_2)$ with the Pt seeds that are left over as a byproduct subpopulation after they were exposed to $Fe(CO)_5$ to form the Pt−Fe_3O_4 heterodimers. The two distinct types of Pt nanoparticle seeds were therefore analyzed using STEM-EDS element mapping in order to identify any possible morphological or compositional differences. Figure 7a, which shows a

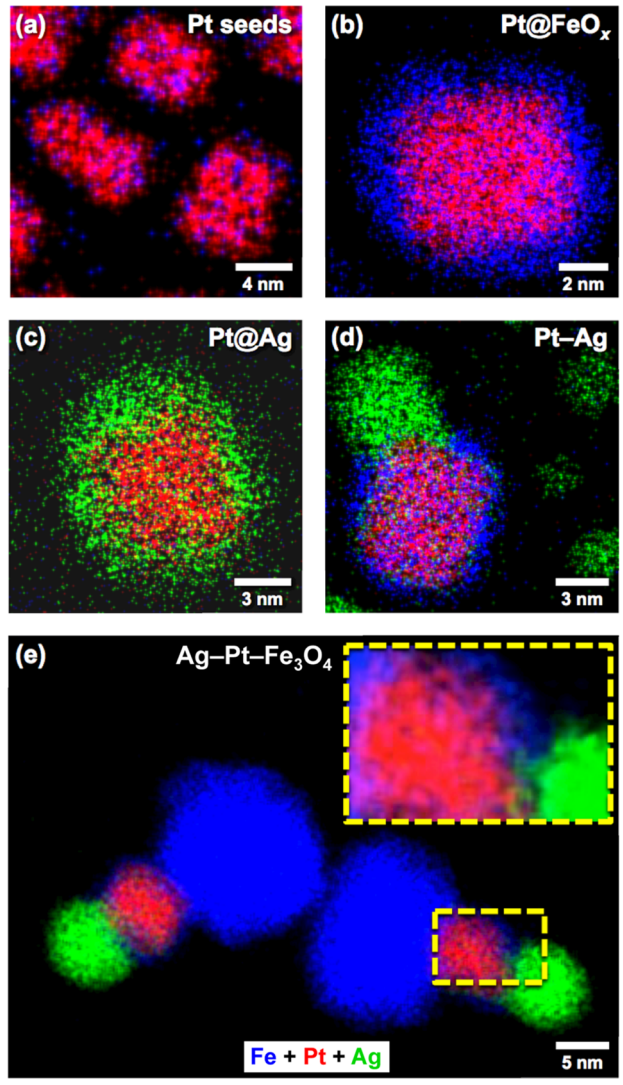

Figure 7. STEM-EDS elemental maps of the (a) as-made Pt seeds, (b) Pt@FeO_x core−shell nanoparticles that are a byproduct of the Pt−Fe_3O_4 synthesis, (c) Pt@Ag core−shell structures, (d) Pt−Ag heterodimer nanoparticles, and (e) Ag−Pt−Fe_3O_4 heterotrimers that exhibit FeO_x islands on the Pt domain.

DOI: 10.1021/jacs.5b10254
J. Am. Chem. Soc. 2015, 137, 15493−15500

STEM-EDS element map of the Pt seed particles that yield the core−shell Pt@Ag nanoparticles, reveals a weak Fe signal distributed homogeneously throughout the Pt nanoparticles. The diffuse Fe signal most likely originates from the small amount of $Fe(CO)_5$ used as a reducing agent in the Pt seed synthesis, which is known to incorporate in small amounts into the nanoparticles and can be further exploited to produce compositionally tunable FePt alloy nanoparticles.[38] The STEM-EDS element map of the Pt seed particles that yield Ag−Pt heterodimers with two distinct lobes, however, shows a clear Fe silhouette enveloping a Pt core (Figure 7b), similar to the amorphous iron shell observed when inadequate precursor ratios are used in the synthesis of Pt−Fe_3O_4.[27]

The data in Figure 7a,b suggest that the presence and location of Fe in the Pt seed is responsible for the different Ag morphologies that are observed. Corresponding STEM-EDS elemental maps for the Pt@Ag core−shell structures and Ag−Pt heterodimers are shown in parts c and d of Figure 7, respectively. The small amount of Fe located on the Pt seeds shown in Figure 7b clearly influences the growth of Ag, resulting in a Ag−Pt heterodimer morphology. In contrast, the Pt nanoparticles shown in Figure 7a, which incorporate only a small amount of Fe and therefore have more exposed Pt to enable nucleation and growth, facilitate the formation of core−shell Pt@Ag structures, as shown in Figure 7c. These results indicate that hybrid nanoparticle morphologies are influenced, and accordingly can be controlled, by carefully engineering the surface chemistry of the nanoparticle seeds. Additionally, this insight helps to explain why Ag grows on Pt−Fe_3O_4 seeds to form the Ag−Pt−Fe_3O_4 heterotrimer, with a distinct Ag domain, rather than the expected core−shell morphology. STEM-EDS element maps of the final Ag−Pt−Fe_3O_4 heterotrimer product (the 14-h sample shown in Figure 2c) further support this idea.

Figure 7e reveals that a Fe-containing shell encompasses most of the Pt domain of the Ag−Pt−Fe_3O_4 heterotrimer, just as in Figure 7b. Additionally, the attached Ag domain is interfaced directly with the Pt surface at the locations where the iron signal is weakest, which again supports the hypothesis that formation of a favorable Ag−Pt interface drives chemoselectivity. Consistent with this, we carried out a similar study involving the growth of Ag on Au nanoparticle seeds as well as Au−Fe_3O_4 heterodimers that were made using the Au nanoparticle seeds (see Figure S8 in the Supporting Information). When Ag was deposited onto the Au−Fe_3O_4 heterodimers, Ag−Au−Fe_3O_4 heterotrimers formed. However, when Ag was deposited onto the Au nanoparticle seeds that had not been previously exposed to iron reagents, Ag−Au alloyed nanoparticles were instead observed. This is consistent with a previous report showing that the presence of a thin iron oxide shell can prevent significant alloying and favor the formation of Au−Ag hybrid particles.[39] These microscopic insights, therefore, suggest that the surface of the noble metal nanoparticle domain is altered with iron oxide deposits formed *in situ* during the seeded growth reaction, and this in turn decreases the accessible surface area of the noble metal nanoparticle domain that is available to anchor coalescence of the second metal domain (Ag in the case of Ag−Pt−Fe_3O_4 heterotrimer formation) after indiscriminate surface nucleation and subsequent migration.

As demonstrated above, subtle differences in the surface compositions of the seed particles, which result from distinct stages of the reaction pathway, can lead to different hybrid nanoparticle morphologies. This, in turn, can lead to distinct properties. For example, Figure S9 (Supporting Information) shows the normalized UV−visible absorption spectra for the as-made 14-h product, which contains predominantly Ag−Pt−Fe_3O_4 heterotrimers, along with Ag−Pt heterodimers. Figure S9 also shows UV−visible absorption spectra for Pt@Ag particles exhibiting a core−shell architecture, as well as spherical Ag nanoparticles with an average diameter (9 ± 3 nm) that matches closely with those that comprise the Ag domains of the Ag−Pt−Fe_3O_4 and Ag−Pt hybrid nanoparticles. Both the Ag nanoparticles and the 14-h hybrid nanoparticle product exhibit a peak in the optical absorption at ∼400 nm, which corresponds to the surface plasmon resonance (SPR) for spherical Ag particles in this size regime.[40] This indicates that the Ag domain of the heterostructured nanoparticles exhibits the plasmonic properties expected for Ag. The Pt@Ag nanoparticles having a core−shell architecture, however, exhibit a blue-shifted SPR peak at ∼350 nm, indicating, as expected, that the Ag−Pt morphology impacts the SPR. These measurements confirm that subtle, but important, differences in synthetic pathways and hybrid nanoparticle morphologies can lead to distinct properties, and therefore, accessing precisely targeted properties requires an in-depth understanding of the synthetic pathway, as detailed here.

■ CONCLUSIONS

Engineering high-order hybrid nanoparticles, such as three-component heterotrimers, with precisely targeted morphologies and functionalities using seeded-growth methods remains a significant challenge. This is due, in part, to the nucleation and growth of a third type of nanoparticle onto a two-component heterodimer seed, which has two distinct surfaces exposed and accessible. Unlike the stepwise reaction sequences used in organic chemistry to construct large complex molecules, the reactions that govern the formation of high-order hybrid nanoparticles are not well understood. In this study, we provided mechanistic insights into the pathway by which Ag−Pt−Fe_3O_4 heterotrimer nanoparticles form. Specifically, the microscopic studies revealed that Ag first nucleates indiscriminately onto both surfaces of the Pt−Fe_3O_4 heterodimer seeds, followed by surface diffusion and coalescence of the Ag domains onto the Pt surface, ultimately forming the final product, Ag−Pt−Fe_3O_4. This observation suggests that the formation of an energetically favorable Ag−Pt interface, relative to Ag−Fe_3O_4, is the driving force for surface-specific, chemoselective growth in heterotrimer nanoparticle formation, which is important knowledge that could be leveraged to improve future efforts to design and synthesize precisely targeted heterotrimer systems. By identifying and understanding the pathway by which the heterotrimers form, new ways of shutting down this pathway to instead favor nonpreferred domain configurations (configurational isomers) may now be possible.[27,41] Additionally, carefully designed control experiments revealed that the morphology of the heterodimer seeds plays an important role in determining the morphology of the final heterotrimer product, providing additional insights for precisely fine-tuning subtle morphological features. Finally, we demonstrated that small deposits on the heterodimer seed surfaces, which emerge during synthesis and often remain unidentified and elusive, can profoundly influence the morphology of the domains added subsequently to these systems. Such knowledge must be considered when designing synthetic strategies for accessing hybrid nanoparticles

DOI: 10.1021/jacs.5b10254
J. Am. Chem. Soc. 2015, 137, 15493−15500

with targeted morphological features. Collectively, these results provide important new insights and guidelines that complement and underpin the growing synthetic framework for constructing high-order hybrid nanoparticles that have diverse applications in areas such as biomedical imaging, solar-energy harvesting, heterogeneous catalysis, photonics, optics, and electronics.

■ ASSOCIATED CONTENT

Supporting Information

The Supporting Information is available free of charge on the ACS Publications website at DOI: 10.1021/jacs.5b10254.

Additional experimental details and supplemental TEM, HRTEM, STEM-EDS elemental maps, and histograms (PDF)

■ AUTHOR INFORMATION

Corresponding Author

*res20@psu.edu

Author Contributions

J.M.H and J.R.M. contributed equally to this work.

Notes

The authors declare no competing financial interest.

■ ACKNOWLEDGMENTS

This work was supported by the U.S. National Science Foundation under grant CHE-1410061 (J.M.H., J.R.M., R.E.S.). DMCR work was supported by the U.S. National Science Foundation under grant CHE-1213439 (J.R.M., M.E.W.). TEM imaging was performed at the Penn State Microscopy and Cytometry facility and HRTEM imaging was performed at the Materials Characterization Lab of the Penn State Materials Research Institute. The authors thank Jennifer Gray and Ke Wang for assistance in collecting the TEM images.

■ REFERENCES

(1) Xu, C.; Xie, J.; Ho, D.; Wang, C.; Kohler, N.; Walsh, E. G.; Morgan, J. R.; Chin, Y. E.; Sun, S. *Angew. Chem., Int. Ed.* **2008**, *47*, 173−176.

(2) Amirav, L.; Oba, F.; Aloni, S.; Alivisatos, A. P. *Angew. Chem., Int. Ed.* **2015**, *54*, 7007−7011.

(3) Amirav, L.; Alivisatos, A. P. *J. Phys. Chem. Lett.* **2010**, *1*, 1051−1054.

(4) Li, G.; Cherqui, C.; Bigelow, N. W.; Duscher, G.; Straney, P. J.; Millstone, J. E.; Masiello, D. J.; Camden, J. P. *Nano Lett.* **2015**, *15*, 3465−3471.

(5) George, C.; Genovese, A.; Casu, A.; Prato, M.; Povia, M.; Manna, L.; Montanari, T. *Nano Lett.* **2013**, *13*, 752−757.

(6) Guo, S.; Zhang, X.; Zhu, W.; He, K.; Su, D.; Mendoza-garcia, A.; Ho, S. F.; Lu, G.; Sun, S. *J. Am. Chem. Soc.* **2014**, *136*, 15026−15033.

(7) Wang, C.; Daimon, H.; Sun, S. *Nano Lett.* **2009**, *9*, 1493−1496.

(8) Carbone, L.; Nobile, C.; De Giorgi, M.; Della Sala, F.; Morello, G.; Pompa, P.; Hytch, M.; Snoeck, E.; Fiore, A.; Franchini, I. R.; Nadasan, M.; Silvestre, A. F.; Chiodo, L.; Kudera, S.; Cingolani, R.; Krahne, R.; Manna, L. *Nano Lett.* **2007**, *7*, 2942−2950.

(9) Grim, J. Q.; Manna, L.; Moreels, I. *Chem. Soc. Rev.* **2015**, *44*, 5897−5914.

(10) Gordon, T. R.; Schaak, R. E. *Chem. Mater.* **2014**, *26*, 5900−5904.

(11) Ye, X.; Reifsnyder Hickey, D.; Fei, J.; Diroll, B. T.; Paik, T.; Chen, J.; Murray, C. B. *J. Am. Chem. Soc.* **2014**, *136*, 5106−5115.

(12) Mokari, T.; Rothenberg, E.; Popov, I.; Costi, R.; Banin, U. *Science* **2004**, *304*, 1787−1790.

(13) Sheldon, M. T.; Trudeau, P. E.; Mokari, T.; Wang, L. W.; Alivisatos, A. P *Nano Lett.* **2009**, *9*, 3676−3682.

(14) Costi, R.; Saunders, A. E.; Elmalem, E.; Salant, A.; Banin, U. *Nano Lett.* **2008**, *8*, 637−641.

(15) Choi, C. L.; Alivisatos, A. P. *Annu. Rev. Phys. Chem.* **2010**, *61*, 369−389.

(16) Skumryev, V.; Stoyanov, S.; Zhang, Y.; Hadjipanayis, G.; Givord, D.; Nogués, J. *Nature* **2003**, *423*, 850−853.

(17) Figuerola, A.; Fiore, A.; Di Corato, R.; Falqui, A.; Giannini, C.; Micotti, E.; Lascialfari, A.; Corti, M.; Cingolani, R.; Pellegrino, T.; Cozzoli, P. D.; Manna, L. *J. Am. Chem. Soc.* **2008**, *130*, 1477−1487.

(18) Lee, J. H.; Jang, J. T.; Choi, J. S.; Moon, S. H.; Noh, S. H.; Kim, J. W.; Kim, J. G.; Kim, I. S.; Park, K. I.; Cheon, J. *Nat. Nanotechnol.* **2011**, *6*, 418−422.

(19) Acharya, K. P.; Khnayzer, R. S.; O'Connor, T.; Diederich, G.; Kirsanova, M.; Klinkova, A.; Roth, D.; Kinder, E.; Imboden, M.; Zamkov, M. *Nano Lett.* **2011**, *11*, 2919−2926.

(20) Schick, I.; Gehrig, D.; Schilmann, A.; Bauer, H.; Panthöfer, M.; Fischer, K.; Strand, D.; Lorenz, S.; Laquai, F.; Tremel, W. *J. Am. Chem. Soc.* **2014**, *136*, 2473−2483.

(21) Buck, M. R.; Schaak, R. E. *Angew. Chem., Int. Ed.* **2013**, *52*, 6154−6176.

(22) Buck, M. R.; Bondi, J. F.; Schaak, R. E. *Nat. Chem.* **2011**, *4*, 37−44.

(23) Read, C. G.; Gordon, T. R.; Hodges, J. M.; Schaak, R. E. *J. Am. Chem. Soc.* **2015**, *137*, 12514−12517.

(24) Bradley, M. J.; Read, C. G.; Schaak, R. E. *J. Phys. Chem. C* **2015**, *119*, 8952−8959.

(25) Wu, H.; Chen, O.; Zhuang, J.; Lynch, J.; Lamontagne, D.; Nagaoka, Y.; Cao, Y. C. *J. Am. Chem. Soc.* **2011**, *133*, 14327−14337.

(26) Zhang, H.; Ding, J.; Chow, G.; Dong, Z. *Langmuir* **2008**, *24*, 13197−13202.

(27) Hodges, J. M.; Biacchi, A. J.; Schaak, R. E. *ACS Nano* **2014**, *8*, 1047−1055.

(28) Wang, C.; Yin, H.; Dai, S.; Sun, S. *Chem. Mater.* **2010**, *22*, 3277−3282.

(29) Zhang, L.; Dou, Y. H.; Gu, H. C. *J. Colloid Interface Sci.* **2006**, *297*, 660−664.

(30) Wu, B.; Zhang, H.; Chen, C.; Lin, S.; Zheng, N. *Nano Res.* **2009**, *2*, 975−983.

(31) Park, J.; An, K.; Hwang, Y.; Park, J.-G.; Noh, H.; Kim, J.; Park, J.; Hwang, N.; Hyeon, T. *Nat. Mater.* **2004**, *3*, 891−895.

(32) Beveridge, J. S.; Stephens, J. R.; Latham, A. H.; Williams, M. E. *Anal. Chem.* **2009**, *81*, 9618−9624.

(33) Beveridge, J. S.; Buck, M. R.; Bondi, J. F.; Misra, R.; Schiffer, P.; Schaak, R. E.; Williams, M. E. *Angew. Chem., Int. Ed.* **2011**, *50*, 9875−9879.

(34) Becker, A. F.; Rosenfeld, G.; Poelsema, B.; Comsa, G. *Phys. Rev. Lett.* **1993**, *70*, 477−480.

(35) Grossmann, a.; Erley, W.; Hannon, J.; Ibach, H. *Phys. Rev. Lett.* **1996**, *77*, 127−130.

(36) Peng, S.; Lei, C.; Ren, Y.; Cook, R. E.; Sun, Y. *Angew. Chem., Int. Ed.* **2011**, *50*, 3158−3163.

(37) Ridelman, Y.; Singh, G.; Popovitz-Biro, R.; Wolf, S. G.; Das, S.; Klajn, R. *Small* **2012**, *8*, 654−660.

(38) Chen, M.; Liu, J. P.; Sun, S. *J. Am. Chem. Soc.* **2004**, *126*, 8394−8395.

(39) Sun, Y.; Foley, J. J.; Peng, S.; Li, Z.; Gray, S. K. *Nano Lett.* **2013**, *13*, 3958−3964.

(40) Cortie, M. B.; Mcdonagh, A. M. *Chem. Rev.* **2011**, *111*, 3713−3735.

(41) Read, C. G.; Biacchi, A. J.; Schaak, R. E. *Chem. Mater.* **2013**, *25*, 4304−4311.

DOI: 10.1021/jacs.5b10254
J. Am. Chem. Soc. 2015, 137, 15493−15500